Design and Kinematic Analysis of a 6-DoF Parallel Robot for Image-guided Surgery

1st Xiyu Wang
School of Intelligent Systems Engineering
Shenzhen Campus of Sun Yat-sen University
Shenzhen, China
wangxy623@mail2.sysu.edu.cn

2nd Yongyin Ye
School of Intelligent Systems Engineering
Shenzhen Campus of Sun Yat-sen University
Shenzhen, China
yeyy33@mail2.sysu.edu.cn

3rd Zhijie Pan
School of Intelligent Systems Engineering
Shenzhen Campus of Sun Yat-sen University
Shenzhen, China
panzhj6@mail2.sysu.edu.cn

4th Jiangnan Wang
School of Intelligent Systems Engineering
Shenzhen Campus of Sun Yat-sen University
Shenzhen, China
wangjn229@mail2.sysu.edu.cn

5th Ruchi Guo
Department of Mathematics
University of California, Irvine
Irvine, USA
ruchig@uci.edu

6th Mengtang Li
School of Intelligent Systems Engineering
Shenzhen Campus of Sun Yat-sen University
Shenzhen, China
limt29@mail.sysu.edu.cn

***Abstract*—Image-guided robot based on medical imaging is extensively utilized in the field of surgery due to its inherent characteristics of enhanced precision and larger accessible workspace than surgeons, resulting in reduced harm to patients. Nevertheless, the robots currently employed in image-guided surgery are either insufficiently stable serial robots or parallel robots that pose difficulties in computing direct kinematics. As an improvement to current robot-assisted surgical systems, a compact six degrees of freedom (DoF) decoupled parallel robot has been proposed and corresponding kinematic model has been established. Furthermore, an algorithm based on Newton iterative method is employed to solve the forward kinematics problem. Finally, simulated neurosurgical experiments are carried out to display the trajectory of motion planning and to verify the correctness of kinematics. Experiment results demonstrate that the proposed parallel robot can achieve satisfactory performance.**

***Index Terms*—Image-guided robot; Parallel robot; Robot kinematics.**

I. Introduction

Image-guided surgery is considered a multidisciplinary field that combines real-time imaging techniques with surgical interventions to enhance the precision and accuracy of surgical procedures. Compared with traditional surgery limited by the inadequacies of human visualization and dexterity, the utilization of various imaging modalities such as CT and MRI offers several potential benefits, including improved surgical accuracy, reduced invasiveness, minimized tissue damage, shorted procedure duration and enhanced patient safety [1]. Hence, it has been widely applied in neurosurgery [2], orthopedics [3] and other medical specialties.

Advances in image-guided surgery are also fueling the drive for robotics as robots augment the capabilities of surgeons and improve the overall surgical workflow. Firstly, robots can provide high levels of precision and accuracy in executing surgical tasks with their ability to perform fine movements and their inherent stability [4]. Moreover, robots can be designed with multiple degrees of freedom and flexible joints, allowing them to access difficult-to-reach areas within a patient's body [4]. Combined medical robotics with existing imaging modalities, several image-guided robots were proposed and proved to be feasible and accurate. Stoianovici designed a 6-DoF robot mounted on a CT-scanner which was distinguished another by its decoupled motion capability [5]. As better imaging quality and less ionizing radiation are provided by MRI, an MR-compatible assistance system named INNOMOTION with five pneumatically driven DoFs and two adjustments for prepositioning was proposed by Melzer [6]. Figure 1 draws the general workflow of image-guided robot system.

Reflecting on the research conducted over the past few decades, the study and development of medical image-guided surgical robots have mostly been associated with robotic arms, which are categorized as serial robots in the field of robotics. However, due to the high accuracy requirement in robotic surgery, parallel robots are superior to their serial counterparts from this aspect. Parallel robots typically have a higher stiffness and rigidity, allowing them to maintain better positional

This project is funded by the Foundation for Shenzhen Science and Technology Program (Grant No. RCBS20221008093104018). Wang, X. and Ye, Y. contributed equally. Li, M., *IEEE Member*, is the corresponding author.

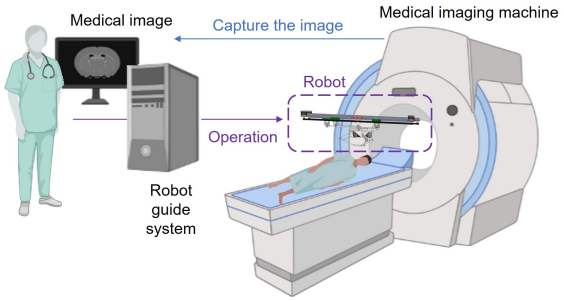

Fig. 1. Illustration of the usage scenario of image-guided robot system.

accuracy and repeatability. Besides, the redundant connections and multiple supporting joints contribute to the ability to withstand external forces and maintain stability even in the event of component failures [7]. Considering aforementioned advantages, researchers developed several parallel robots for image-guided surgeries. Su proposed a reconfigurable manipulator utilizing parallel mechanism under MRI guidance [8]. Li developed a 6-DoF parallel robotic assistant including a remotely actuated needle driver module and a needle alignment module for MRI-guided low back pain injection [9].

Nevertheless, parallel robots have not gained widespread recognition in the field of image-guided surgery. One possible reason behind is the challenging nature of solving their forward kinematics, which is pivotal in feedback control and motion planning. As a result of the intricate geometry and redundancy of parallel robots, the mathematical equations required to accurately compute the forward kinematics become highly nonlinear and often involve complex trigonometric functions [10]. According to the existing literature, the current methods for the parallel robot's forward kinematics can be classified into four categories: analytical approaches with highly coupled nonlinear equations that hard to solve [11], numerical methods with the difficulty of choosing the initial value [12], extra-sensors approaches limited by the measurement and assembly error [12], artificial intelligence methods in dire need of investigation but hard to balance the computational accuracy and efficiency [13].

To tackle the aforementioned issues, this paper proposes a novel robot system for image-guided surgery applications in the future, combining the stability advantage of parallel robots and the large-workspace feature of serial robots. This device can promisingly serve as a versatile robotic platform for image-guided surgery, rather than being specific to a particular type of procedure. The rest of the paper is arranged as follows. Section II introduces the mechanical design of the proposed robot, along with geometry and mobility analysis. Section III presents inverse kinematics modeling, followed by forward kinematics analysis using Newton numerical method. Section IV establishes simulation verification of the parallel robot and Section V draws conclusive remarks.

II. Mechanical Design

A. Robot Description

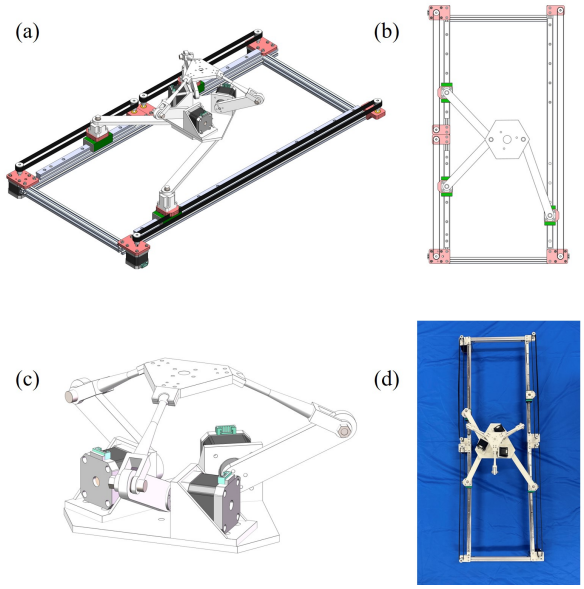

Fig. 2. (a) CAD design of the proposed robot. (b) Bottom layer: a sliding rail parallel module. (c) Top layer: a 3-RRS parallel module. (d) Prototype of the proposed robot.

As shown in Fig.2, the robot proposed in this paper includes two modules that effectively expand its operational range, allowing for a larger workspace while occupying a smaller system size. The bottom layer is a sliding rail parallel module controlled by three actuators to provide the hexagonal base with translations along x and y directions and rotation around z direction. This hexagonal platform is connected by two rods from one side of the rails at a common joint and one single rod from the other side at a symmetrical position. With certain combinations of actuator displacements, translations and rotations of the hexagonal platform can be achieved via the bottom 3-PRR module. The top layer features a classical 3-RRS architecture. Each chain consists of two links with one spherical passive joint, one revolute passive joint and one revolute active joint. The three revolute active joints are controlled to actuate the end effector platform, achieving rotations around x and y directions and translation along z direction. A noteworthy feature of the proposed robot is that the bottom and the top layers are fundamentally decoupled, facilitating the robot kinematic modeling.

B. Mobility Analysis

The mobility of a parallel robot can be calculated by using Grübler's formula:

$$F = m(N - 1 - J) + \sum_{i=1}^{n} f_i$$

where m represents the degrees of freedom associated with the motion space, N denotes the total number of rigid bodies

present in the mechanism, J represents the overall count of joints within the system, and each joint i possesses a degree of freedom denoted by f_i.

As the proposed parallel robot is eventually a decoupled system, the system degree of freedom can be analyzed with respect to two distinct modules. The bottom 3-PRR planar parallel module works in a $m = 3$ space, $N = 8$, $J = 9$ and $\sum_{i=1}^{n} f_i = 9$. Then the DoF of the bottom module is $F = m(N - 1 - J) + \sum_{i=1}^{n} f_i = 3(8 - 1 - 9) + 9 = 3$. From a visual perspective, the operation of the motors induces movement in the three joints, thereby causing positional adjustments of the platform. Consequently, this leads to translational displacements along the x and y axes, as well as rotational motion around the z axis. And the top 3-RRS parallel module works in a $m = 6$ space, $N = 8$, $J = 9$ and $\sum_{i=1}^{n} f_i = 15$. Hence the DoF of the top module is $F = m(N - 1 - J) + \sum_{i=1}^{n} f_i = 6(8 - 1 - 9) + 15 = 3$. In a similar manner, the motors actuate the movement of the three joints, causing the passive joints to induce positional changes in the platform. This results in rotational motion along the x and y axes, as well as translational displacement along the z axis. Conclusively, the entire system is capable of achieving 6-DoF motions for the end effector platform.

III. Kinematic Analysis

Analogous to the previous section, we also leverage the system's partially decoupled nature to separately analyze the kinematics of the bottom and top modules.

A. The Bottom 3-PRR Sliding Rail Parallel Module

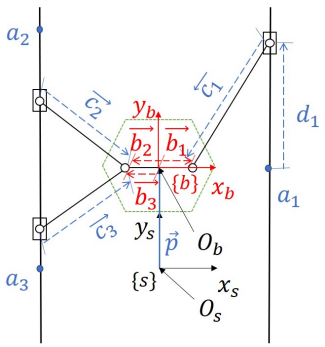

Fig. 3. Kinematic diagram of the bottom 3-PRR parallel module.

1) Inverse Kinematics: The configuration of the bottom module can be explained by the loop closure method. As shown in Fig.3, a fixed frame $\{s\}$ is positioned at the spot O_s, while the body frame $\{b\}$ is positioned at the spot O_b on the hexagonal base. L refers to the width between the two rails. The distance moved by each active joint relative to the initial reference vector $\boldsymbol{a}_i$ is represented as $\boldsymbol{d}_i, i = 1, 2, 3$. Denote the coordinate representation of the origin of $\{b\}$ in $\{s\}$ by $\boldsymbol{p}$. Let φ be rotational angle of the body frame $\{b\}$ relative to the fixed frame $\{s\}$. Further, define $\boldsymbol{c}_i$ as a vector aligned with the direction of the rod and having the same length as the rod, and $\boldsymbol{b}_i$ as the vector from O_b to the joint on the hexagonal platform. Note that both $\boldsymbol{b}_2$ and $\boldsymbol{b}_3$ refer to the identical vector. The inverse kinematics problem is to determine $\boldsymbol{d} = (d_1, d_2, d_3)$ from the given values of $\boldsymbol{T}_{sb} \in SE(3)$. The homogeneous coordinate transformation matrix $\boldsymbol{T}_{sb}$ from the fixed frame $\{s\}$ to the moving coordinate frame $\{b\}$ is:

$$\boldsymbol{T}_{sb} = \begin{bmatrix} \boldsymbol{R}_{sb} & \boldsymbol{p} \\ 0 & 1 \end{bmatrix}, \boldsymbol{R}_{sb} = \begin{bmatrix} c\varphi & -s\varphi & 0 \\ s\varphi & c\varphi & 0 \\ 0 & 0 & 1 \end{bmatrix}, \boldsymbol{p} = \begin{bmatrix} p_x \\ p_y \\ 0 \end{bmatrix}$$

where s and c stand for sin and cos respectively, $\boldsymbol{R}_{sb}$ is the rotation matrix defining the orientation of the body frame $\{b\}$ with respect to the fixed frame $\{s\}$. From these definitions, clearly we have:

$$\boldsymbol{d}_i = \boldsymbol{p} + \boldsymbol{b}_i - \boldsymbol{a}_i - \boldsymbol{c}_i \tag{1}$$

Note that $\boldsymbol{a}_i$, $\boldsymbol{b}_i$ and $||\boldsymbol{c}_i||$ are all constant, and all the vectors are expressed in $\{s\}$-frame coordinates with the exception of $\boldsymbol{b}_i$. So combining with the rotation matrix, Eq.(1) can be illustrated as follow:

$$\begin{bmatrix} d_{ix} \\ d_{iy} \\ 0 \end{bmatrix} = \begin{bmatrix} p_{ix} \\ p_{iy} \\ 0 \end{bmatrix} + \begin{bmatrix} c\varphi & -s\varphi & 0 \\ s\varphi & c\varphi & 0 \\ 0 & 0 & 1 \end{bmatrix} \begin{bmatrix} b_{ix} \\ b_{iy} \\ 0 \end{bmatrix} - \begin{bmatrix} a_{ix} \\ a_{iy} \\ 0 \end{bmatrix} - \begin{bmatrix} c_{ix} \\ c_{iy} \\ 0 \end{bmatrix} \tag{2}$$

for $i = 1, 2, 3$. Also, since $||\boldsymbol{c}_i||$ is constant and $\boldsymbol{d}_{ix} = 0$, we have

$$d_{ix} = p_x + c\varphi b_{ix} - s\varphi b_{iy} - a_{ix} - c_{ix} = 0 \tag{3}$$

$$d_{iy} = p_y + s\varphi b_{ix} + c\varphi b_{iy} - a_{iy} - c_{iy} \tag{4}$$

$$c_{ix}^2 + c_{iy}^2 = ||\boldsymbol{c}_i||^2 \tag{5}$$

for $i = 1, 2, 3$. Formulated as above, the inverse kinematics of the bottom sliding rail module is readily calculable: given values for (p_x, p_y, φ), the active joints' displacement can be directly computed from Eqs.(3)-(5).

2) Forward Kinematics: On the contrary, the forward kinematics problem involves determining the position and orientation of the body frame $\boldsymbol{T}_{sb}$, given the known displacement of the active joints $\boldsymbol{d} = (\boldsymbol{d}_1, \boldsymbol{d}_2, \boldsymbol{d}_3)$. By incorporating the tangent half-angle substitution, Eqs.(3)-(5) can be reformulated as polynomial equations in terms of t as follows:

$$d_{ix} + a_{ix} + c_{ix} = p_x + \frac{1 - t^2}{1 + t^2} b_{ix} - \frac{2t}{1 + t^2} b_{iy} \tag{6}$$

$$d_{iy} + a_{iy} + c_{iy} = p_y + \frac{2t}{1 + t^2} b_{ix} + \frac{1 - t^2}{1 + t^2} b_{iy} \tag{7}$$

$$c_{ix}^2 + c_{iy}^2 = ||\boldsymbol{c}_i||^2 \tag{8}$$

$$t = \tan(\varphi/2) \tag{9}$$

for $i = 1, 2, 3$. Through some mathematical manipulations, Eqs.(6)-(9) can be reduced to a simplified univariate 8th-degree polynomial with respect to t, indicating the forward kinematics of the bottom module can have at most eight solutions. But due to the specific design of the bottom module, where the two rods on the left are of equal length and the range of motion for the rod on the right is limited to the upper

plane, the eight possible solutions can be reduced to two. Hence, when utilizing forward kinematics to determine the pose of the end-effector $\boldsymbol{T}_{sb}$ under the current displacements of the active joints, it is important to take into account the robot's previous state in order to eliminate alternative forward kinematics solutions. By selecting a solution that is close to the previous state, we can estimate the forward kinematics of $\boldsymbol{T}_{sb}$ accurately for the current configuration.

B. The Top 3-RRS Parallel Module

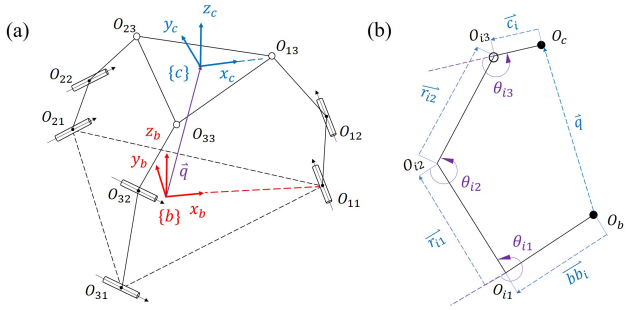

Fig. 4. (a) Kinematic diagram of the top 3-RRS parallel module. (b) Simplified model of a closed-loop joint system.

1) Inverse Kinematics: Compared to the distinctive design of the bottom layer, the top 3-RRS parallel module is a more commonly encountered mechanism [14]. As shown in Fig.4, the body frame $\{b\}$ is the same as the bottom module, while the $\{c\}$-frame coordinate system is attached at the spot O_c on the moving platform. $\triangle O_{11}O_{21}O_{31}$ and $\triangle O_{13}O_{23}O_{33}$ are two equilateral triangles. Denote the vectors from O_b to O_{i1} by $\boldsymbol{bb}_i$, for $i = 1, 2, 3$. And the x_b-axis is chosen to be along with $\boldsymbol{bb}_1$. Similarly, $\boldsymbol{c}_i$ represent the vectors from O_c to O_{i3}, while x_c-axis is chosen to be along with $\boldsymbol{c}_1$. The position vector that defines the location of the upper coordinate frame $\{c\}$ with respect to the body frame $\{b\}$ is $\boldsymbol{q}$. $\boldsymbol{r}_{i1} = \overrightarrow{O_{i1}O_{i2}}$ are the lower limb vectors, controlling by actuators. $\boldsymbol{r}_{i2} = \overrightarrow{O_{i2}O_{i3}}$ represent the upper limb vectors, but they are passive joints' parameters. Let $\boldsymbol{\theta}_{ij}$, for $i = 1, 2, 3, j = 1, 2, 3$ denote the angle of a joint, while $\boldsymbol{\psi} = (\psi_x, \psi_y, \psi_z)$ corresponds to the angle of rotation. The inverse kinematics problem is to determine $\boldsymbol{\theta}_{i1} = (\theta_{11}, \theta_{21}, \theta_{31})$ from the given values of $\boldsymbol{T}_{bc} \in SE(3)$.Then the homogeneous coordinate transformation matrix $\boldsymbol{T}_{bc}$ from the body frame $\{b\}$ to the moving coordinate frame $\{c\}$ can be shown:

$$\boldsymbol{T}_{bc} = \begin{bmatrix} \boldsymbol{R}_{bc} & \boldsymbol{q} \\ 0 & 1 \end{bmatrix}, \boldsymbol{q} = \begin{bmatrix} q_x \\ q_y \\ q_z \end{bmatrix},$$

$$\boldsymbol{R}_{bc} = \boldsymbol{R}_x \cdot \boldsymbol{R}_y \cdot \boldsymbol{R}_z$$

$$= \begin{bmatrix} 1 & 0 & 0 \\ 0 & c\psi_x & -s\psi_x \\ 0 & s\psi_x & c\psi_x \end{bmatrix} \begin{bmatrix} c\psi_y & 0 & s\psi_y \\ 0 & 1 & 0 \\ -s\psi_y & 0 & c\psi_y \end{bmatrix} \begin{bmatrix} c\psi_z & -s\psi_z & 0 \\ s\psi_z & c\psi_z & 0 \\ 0 & 0 & 1 \end{bmatrix}$$

where $\boldsymbol{R}_{bc}$ is the rotation matrix defining the orientation of the upper frame $\{c\}$ with respect to the body frame $\{b\}$.

Due to the constraints imposed by the geometric structure, the top layer has only three parameters q_z ψ_x ψ_y that can be freely adjusted, while the remaining three parameters q_x q_y ψ_z are determined by the bottom module, as mentioned above. Therefore, the following will elucidate some constraints on the parameters in order to analyze kinematics.

$$\begin{aligned} \overrightarrow{O_bO_{13}} &= \boldsymbol{q} + \boldsymbol{c}_1 \Rightarrow \begin{bmatrix} O_{13,x} & O_{13,y} & O_{13,z} \end{bmatrix}^T \\ &= \begin{bmatrix} O_{c,x} & O_{c,y} & O_{c,z} \end{bmatrix}^T + \boldsymbol{R}_{bc} \cdot \boldsymbol{R}_z(\alpha_1) \begin{bmatrix} r_c & 0 & 0 \end{bmatrix}^T \end{aligned} \tag{10}$$

$$\begin{aligned} \overrightarrow{O_bO_{23}} &= \boldsymbol{q} + \boldsymbol{c}_2 \Rightarrow \begin{bmatrix} O_{23,x} & O_{23,y} & O_{23,z} \end{bmatrix}^T \\ &= \begin{bmatrix} O_{c,x} & O_{c,y} & O_{c,z} \end{bmatrix}^T + \boldsymbol{R}_{bc} \cdot \boldsymbol{R}_z(\alpha_2) \begin{bmatrix} r_c & 0 & 0 \end{bmatrix}^T \end{aligned} \tag{11}$$

$$\begin{aligned} \overrightarrow{O_bO_{33}} &= \boldsymbol{q} + \boldsymbol{c}_3 \Rightarrow \begin{bmatrix} O_{33,x} & O_{33,y} & O_{33,z} \end{bmatrix}^T \\ &= \begin{bmatrix} O_{c,x} & O_{c,y} & O_{c,z} \end{bmatrix}^T + \boldsymbol{R}_{bc} \cdot \boldsymbol{R}_z(\alpha_3) \begin{bmatrix} r_c & 0 & 0 \end{bmatrix}^T \end{aligned} \tag{12}$$

where r_c is the radius of the circumscribed circle of the top layer and $\alpha_{1,2,3} = 0, \frac{2\pi}{3}, \frac{4\pi}{3}$. From Eqs.(10)-(12) can we have the following results:

$$O_{c,y} = -r_c(c\psi_z s\psi_x s\psi_y + c\psi_x s\psi_z) \tag{13}$$

$$O_{c,x} = -\frac{r_c}{2}(c\psi_y c\psi_z - c\psi_x c\psi_z + s\psi_x s\psi_y s\psi_z) \tag{14}$$

$$\psi_z = \tan^{-1}(\frac{-s\psi_x s\psi_y}{c\psi_x + c\psi_y}) \tag{15}$$

for $c\psi_x + c\psi_y \neq 0$. From these definitions, clearly we have

$$\boldsymbol{q} + \boldsymbol{c}_i = \boldsymbol{bb}_i + \boldsymbol{r}_{i1} + \boldsymbol{r}_{i2} \tag{16}$$

for $i = 1, 2, 3$. Then using the right-hand side of the Eq.(16) and resolving into x, y and z components, we have:

$$x : ||\boldsymbol{r}_{i2}||c\theta_{i2}c\alpha_i = O_{i3,x} - c\alpha_i(r_b + ||\boldsymbol{r}_{i1}||c\theta_{i1}) \tag{17}$$

$$y : ||\boldsymbol{r}_{i2}||c\theta_{i2}s\alpha_i = O_{i3,y} - s\alpha_i(r_b + ||\boldsymbol{r}_{i1}||c\theta_{i1}) \tag{18}$$

$$z : ||\boldsymbol{r}_{i2}||s\theta_{i2} = -O_{i3,z} - ||\boldsymbol{r}_{i1}||s\theta_{i1} \tag{19}$$

for $i = 1, 2, 3$. r_b is the radius of the circumscribed circle of the bottom layer. By applying certain mathematical operations to Eq.(17) and Eq.(19), the following results can be derived:

$$\theta_{i1} = 2tan^{-1}(\frac{-B_i \pm \sqrt{A_i^2 + B_i^2 - C_i^2}}{C_i - A_i}) \tag{20}$$

where

$$A_i = 2||\boldsymbol{r}_{i1}||c\alpha_i(r_b c\alpha_i - O_{i3,x})$$

$$B_i = 2||\boldsymbol{r}_{i1}||O_{i3,z}c^2\alpha_i$$

$$C_i = O_{i3,x}^2 - 2r_b O_{i3,x}c\alpha_i + c^2\alpha_i(r_b^2 + ||\boldsymbol{r}_{i1}||^2 - ||\boldsymbol{r}_{i2}||^2 + O_{i3,z}^2)$$

for $C_i - A_i \neq 0, i = 1, 2, 3$. As stated above, the inverse kinematics of the top 3-RRS parallel module can be easily calculated. Given the values for (ψ_x, ψ_y, q_z), the displacements of the active joints can be directly computed using Eq.(20).

2) Forward Kinematics: In forward kinematics, the goal is to find the configuration of the end-effector $\boldsymbol{T}_{bc} \in SE(3)$, given the values of the active joints $\boldsymbol{\theta}_{i1}$, for $i = 1, 2, 3$. However, since multiple sets of passive joints $\boldsymbol{\theta}_{i2}$, for $i = 1, 2, 3$, corresponding to the same combination of active joints but different end-effector configurations, it is necessary to solve for the passive joints first in order to determine a unique end-effector configuration.

$$D_1 = ||\boldsymbol{bb}_1 + \boldsymbol{r}_{11} + \boldsymbol{r}_{12} - (\boldsymbol{bb}_2 + \boldsymbol{r}_{21} + \boldsymbol{r}_{22})||^2 - 3r_c^2 \quad (21)$$

$$D_2 = ||\boldsymbol{bb}_1 + \boldsymbol{r}_{11} + \boldsymbol{r}_{12} - (\boldsymbol{bb}_3 + \boldsymbol{r}_{31} + \boldsymbol{r}_{32})||^2 - 3r_c^2 \quad (22)$$

$$D_3 = ||\boldsymbol{bb}_2 + \boldsymbol{r}_{21} + \boldsymbol{r}_{22} - (\boldsymbol{bb}_3 + \boldsymbol{r}_{31} + \boldsymbol{r}_{32})||^2 - 3r_c^2 \quad (23)$$

Eqs.(21)-(23) describe the geometric constraints of the top module, which can be transformed into expressions involving the passive joints variables $\boldsymbol{\theta}_{i2}$ combining Eq.(24):

$$\begin{aligned} \boldsymbol{r}_{12} &= \begin{bmatrix} ||\boldsymbol{r}_{12}||c\theta_{12} \\ 0 \\ -||\boldsymbol{r}_{12}||s\theta_{12} \end{bmatrix}, \boldsymbol{r}_{22} = \begin{bmatrix} -\frac{1}{2}||\boldsymbol{r}_{22}||c\theta_{22} \\ \frac{\sqrt{3}}{2}||\boldsymbol{r}_{22}||c\theta_{22} \\ -||\boldsymbol{r}_{22}||s\theta_{22} \end{bmatrix}, \\ \boldsymbol{r}_{32} &= \begin{bmatrix} -\frac{1}{2}||\boldsymbol{r}_{32}||c\theta_{32} \\ -\frac{\sqrt{3}}{2}||\boldsymbol{r}_{32}||c\theta_{32} \\ -||\boldsymbol{r}_{32}||s\theta_{32} \end{bmatrix} \end{aligned} \quad (24)$$

To address the issue of multiple solutions in forward kinematics and achieve motion planning, it is necessary to select a solution that closely matches the desired trajectory from the multiple solutions. In this process, similar to the Newton's method for finding the closest solution [15], an iterative computation is performed to select the solution that converges to the correct one. Firstly, we need to establish an iterative equation for the given problem in $\boldsymbol{\theta}_{i2} = (\theta_{12}, \theta_{22}, \theta_{32})$:

$$\boldsymbol{\theta}_{i2}^{(k+1)} = \boldsymbol{\theta}_{i2}^{(k)} - \boldsymbol{J}^{-1}\boldsymbol{F}(\boldsymbol{\theta}_{i2}^{(k)}) \quad (25)$$

where

$$\boldsymbol{F} = \begin{bmatrix} D_1 \\ D_2 \\ D_3 \end{bmatrix}, \boldsymbol{J} = \begin{bmatrix} \frac{\partial D_1}{\partial \theta_{12}} & \frac{\partial D_1}{\partial \theta_{22}} & \frac{\partial D_1}{\partial \theta_{32}} \\ \frac{\partial D_2}{\partial \theta_{12}} & \frac{\partial D_2}{\partial \theta_{22}} & \frac{\partial D_2}{\partial \theta_{32}} \\ \frac{\partial D_3}{\partial \theta_{12}} & \frac{\partial D_3}{\partial \theta_{22}} & \frac{\partial D_3}{\partial \theta_{32}} \end{bmatrix}$$

The matrix $\boldsymbol{J}$ represents the Jacobian matrix of the top 3-RRS parallel module, establishing the relationship between the velocity of the moving platform and the driving angles of the top parallel module when the passive angles $\boldsymbol{\theta}_{i2} = (\theta_{12}, \theta_{22}, \theta_{32})$ are utilized as driving angles [16]. The forward kinematics solution that corresponds to the actual motion can therefore be obtained. Detailed workflow is shown in Fig.5.

IV. Simulation Verification

When the parallel robot is processing, the trajectory tracking of the proposed parallel robot needs to be recorded during the processing experiment to validate the accuracy of forward kinematics. At first, the motion planning of the bottom 3-PRR parallel module is carried out in a simulated neurosurgical

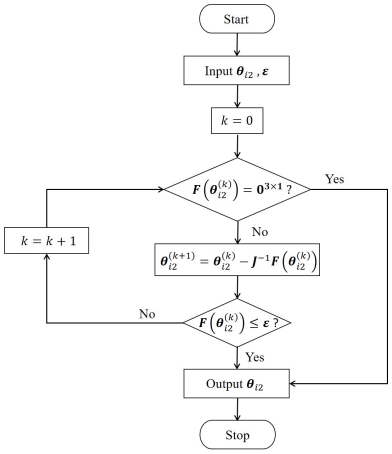

Fig. 5. Flowchart for Newton method in solving for passive joints.

procedure and the displacement tracking errors between the commanded position trajectory and simulated position trajectory are shown. Then, the top 3-RRS parallel module also undergoes the same experiment and the puncture needle is introduced into the experiment to complete the entire process of motion planning and surgical puncture. Robot specification parameters are listed in Table I.

TABLE I
ROBOT SPECIFICATION PARAMETER

Parameter	value(mm)	Parameter	value(mm)
r_b	55.4256	$\|\|\boldsymbol{c}_1\|\|$	250
r_c	60	$\|\|\boldsymbol{c}_2\|\|$	200
$\|\|\boldsymbol{r}_{ij}\|\|$	200	$\|\|\boldsymbol{c}_3\|\|$	200
L	320	$\|\|\boldsymbol{b}_i\|\|$	50

As depicted in Fig.6(a), considering only the movement of the bottom module, a trajectory is defined from the initial position to the target position. By employing inverse kinematics, the displacement of the active joints are calculated, representing the actual motor control displacement in real scenarios. Subsequently, forward kinematics is used to validate the position that the bottom layer will reach in practical circumstances. After conducting a comparative analysis of trajectory errors, as illustrated in Fig.6, the average positional error p_x of the bottom module is 0.322 mm, with an average positional error p_y of 0.187 mm. Additionally, the average angular error φ is calculated to be 0.393°.

Fig.7(a) demonstrates the sequence in which the top layer initiates its movement after the bottom module reaches the target position and remains stationary. Simultaneously, a final simulation of needle insertion is performed. Following a similar methodology applied to the bottom layer, the active joints' variations of the top module are computed using inverse kinematics, and the accuracy of the end-effector pose is then verified using forward kinematics. As shown in Fig.7(b), the additional three degrees of freedom provided by the top module exhibit the following average errors: 0.0024mm in the

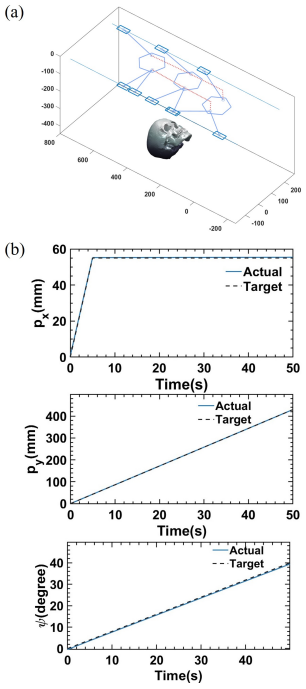

Fig. 6. (a) Tracking trajectory of the bottom parallel module. (b) Comparison between the commanded position trajectory and simulated position trajectory of the bottom parallel module.

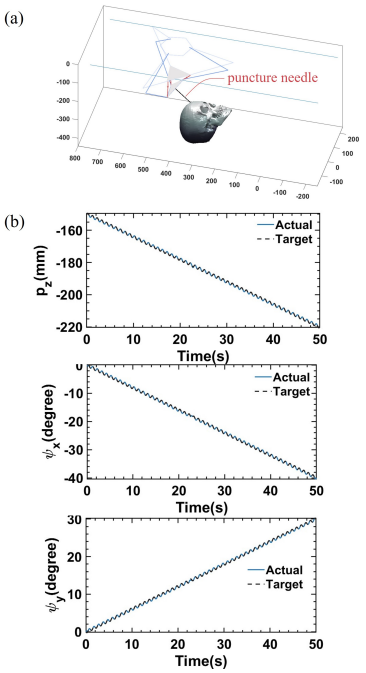

Fig. 7. (a) Tracking trajectory of the top parallel module and needle insertion. (b) Comparison between the commanded position trajectory and simulated position trajectory of the top parallel module.

q_z direction, 0.008° in the ψ_x direction, and 0.0046° in the ψ_y direction.

V. Conclusion

The present study introduces a 6-DoF parallel robot specifically designed for image-guided surgeries. It incorporates a rail sliding architecture to expand the workspace and a mobile module to offer steady and dexterous end-effector configurations. The robot consists of two modules that utilize the Newton method in conjunction with the previous state to address the forward kinematics problem. Simulation tests confirm the feasibility and tracking accuracy of the motion planning. The proposed robot demonstrates versatility and can be effectively applied to a wide range of image-guided surgeries, making it a universal image-guided surgical robot.

Future work encompasses prototype manufacturing and further optimization of the forward kinematics solution, thereby laying the groundwork for subsequent research on the proposed parallel robot.

References

[1] F. Jolesz, *Intraoperative Imaging and Image-Guided Therapy*. Springer New York, 1 2014.

[2] J. Shapey, T. Dowrick, and et al., "Integrated multi-modality image-guided navigation for neurosurgery: open-source software platform using state-of-the-art clinical hardware." *International journal of computer assisted radiology and surgery*, vol. 16, no. 8, p. 1347–1356, 2021.

[3] X. Fan, Q. Zhu, P. Tu, L. Joskowicz, and X. Chen, "A review of advances in image-guided orthopedic surgery," *Physics in medicine and biology*, vol. 68, no. 2, 2023.

[4] R. H. Kassamali and B. Ladak, "The role of robotics in interventional radiology: current status." *Quantitative imaging in medicine and surgery*, vol. 5, no. 3, p. 340–343, 2015.

[5] D. Stoianovici, K. Cleary, A. Patriciu, D. Mazilu, A. Stanimir, N. Craciunoiu, V. Watson, and L. Kavoussi, "Acubot: a robot for radiological interventions," *IEEE Transactions on Robotics and Automation*, vol. 19, no. 5, pp. 927–930, 2003.

[6] A. Melzer, B. Gutmann, T. Remmele, R. Wolf, A. Lukoscheck, M. Bock, H. Bardenheuer, and H. Fischer, "Innomotion for percutaneous image-guided interventions," *IEEE Engineering in Medicine and Biology Magazine*, vol. 27, no. 3, pp. 66–73, 2008.

[7] C. Gosselin and J.-P. Merlet, *Parallel Robots: Architecture, Modeling, and Design*. Springer Berlin Heidelberg, 2020, pp. 1–6.

[8] H. Su, I. I. Iordachita, X. Yan, G. A. Cole, and G. S. Fischer, "Reconfigurable mri-guided robotic surgical manipulator: Prostate brachytherapy and neurosurgery applications," in *2011 Annual International Conference of the IEEE Engineering in Medicine and Biology Society*, 2011, pp. 2111–2114.

[9] G. Li, N. A. Patel, W. Liu, D. Wu, K. Sharma, K. Cleary, J. Fritz, and I. Iordachita, "A fully actuated body-mounted robotic assistant for mri-guided low back pain injection," in *2020 IEEE International Conference on Robotics and Automation (ICRA)*, 2020, pp. 5495–5501.

[10] J.-P. Merletl, *Parallel Robots*. Springer Dordrecht, 7 2006.

[11] E. G. Kalajahi, M. Mahboubkhah, and A. Barari, "Numerical versus analytical direct kinematics in a novel 4-dof parallel robot designed for digital metrology," *IFAC-PapersOnLine*, vol. 54, no. 1, pp. 181–186, 2021.

[12] Q. Zhu and Z. Zhang, "An efficient numerical method for forward kinematics of parallel robots," *IEEE Access*, vol. 7, pp. 128 758–128 766, 2019.

[13] A. Prado, H. Zhang, and S. K. Agrawal, "Artificial neural networks to solve forward kinematics of a wearable parallel robot with semi-rigid links," in *2021 IEEE International Conference on Robotics and Automation (ICRA)*, 2021, pp. 14 524–14 530.

[14] H. Tetik, "Modelling and control of a 3-rrs parallel manipulator," 2016.

[15] Y. Ye, J. Yuan, J. Zhang, X. Wu, X. Wang, B. Ding, and M. Li, "Kinematic modeling of an mri-compatible concentric steerable needle robot based on screw theory," in *2022 China Automation Congress (CAC)*. IEEE, 2022, pp. 1361–1366.

[16] Y. Du, R. Li, D. Li, and S. Bai, "An ankle rehabilitation robot based on 3-rrs spherical parallel mechanism," *Advances in Mechanical Engineering*, vol. 9, 2017.